Comparative Study of Interior Permanent Magnet, Induction, and Switched Reluctance Motor Drives for EV and HEV Applications

Zhi Yang, Fei Shang, *Student Member, IEEE*, Ian P. Brown, *Member, IEEE*, and Mahesh Krishnamurthy, *Senior Member, IEEE*

Abstract—With rapid electrification of transportation, it is becoming increasingly important to have a comprehensive understanding of criteria used in motor selection. This paper presents the design and comparative evaluation for an interior permanent magnet synchronous motor (IPMSM) with distributed winding and concentrated winding, induction motor (IM), and switched reluctance motor (SRM) for an electric vehicle (EV) or hybrid electric vehicle (HEV) application. A fast finite element analysis (FEA) modeling approach is addressed for IM design. To account for highly nonlinear motor parameters and achieve high motor efficiency, optimal current trajectories are obtained by extensive mapping for IPMSMs and IM. Optimal turn-ON and turn-OFF angles with current chopping control and angular position control are found for SRM. Additional comparison including noise vibration and harshness (NVH) is also highlighted. Simulation and analytical results show that each motor topology demonstrates its own unique characteristic for EVs/HEVs. Each motor's highest efficiency region is located at different torque-speed regions for the criteria defined. Stator geometry, pole/slot combination, and control strategy differentiate NVH performance.

Index Terms—Comparative study, electric vehicle (EV) and hybrid electric vehicle (HEV), induction motor (IM), noise vibration and harshness (NVH), permanent magnet motor, switched reluctance motor (SRM).

I. INTRODUCTION

DUE TO increased fuel efficiency and lower cost/mile feature, electric vehicles (EV) and hybrid electric vehicles (HEV) have received increasing attention. To meet this demand, EV and HEV motors, which form the core energy conversion components, should not only satisfy specific requirements in performance and efficiency but also vibration, cost, etc. [1]–[4].

Permanent magnet synchronous motors (PMSM) have dominated the traction motor market for EV/HEV application recently. They can be designed to operate over wide torque-speed range with superior torque density and power density. The limitations of this topology are cost and availability of rare-earth material used in permanent magnet. Other commonly used motor topologies include induction motor (IM) and switched reluctance motor (SRM). An IM has no magnet and is characterized as robust. The limitation of this topology may lie in the cooling system since heat is generated both in rotor and stator side. SRM does not depend on permanent magnets and is exceptionally robust, making it suitable for harsh environments and fault-tolerant operation. However, high-acoustic noise and low-power factor have been some of the major challenges. In addition, SRM drives may need customized inverter and a higher number of power cables to enable independent phase winding on the stator.

Comparisons have been proposed to indicate the merit of each motor topology for EV and HEV application. Researchers in [5] and [6] have presented efficiency maps of the IM, SRM, and PMSM with a general trend. In [7], the authors have analyzed second generation Prius-IPMSM and assessed alternative spoke-type IPMSM and IM. However, the analysis based on fixed phase current angle control over the full torque-speed range may result in nonoptimal operating control. Pellegrino *et al.* have presented a comparison of IPMSM and IM in terms of output power and efficiency over the standard New European Driving Cycle [8]. Similar work has been done in [9]. In [10], authors have claimed that impact of efficiency distribution on fuel consumption is small after comparing IM, PMSM, and SRM. However, in literature, very few papers have provided a comprehensive side-by-side comparison among different traction motor topologies for EV or HEV applications, especially for noise vibration and harshness (NVH) point of view. This paper presents a comparative evaluation of the selected motors topologies including IPMSM, IM, and SRM. Motor efficiency and NVH are the main focus of the comparison among all the candidates. A fast finite element analysis (FEA) modeling approach is adopted for IM over full torque-speed range considering saturation effect and optimal current trajectory control is taking into account for highly nonlinear motor parameters.

In order to address the above-mentioned issues, it becomes necessary to design and conduct a thorough comparison and assessment of candidate motor topologies, including IPMSM with distributed winding, IPMSM with concentrated winding, IM, and SRM. However, it is impractical to build prototypes for all the competitors and compared with experimental results. Moreover, all the design and evaluation results are acquired from FEA in ANSYS environment including RMxprt (magnetic
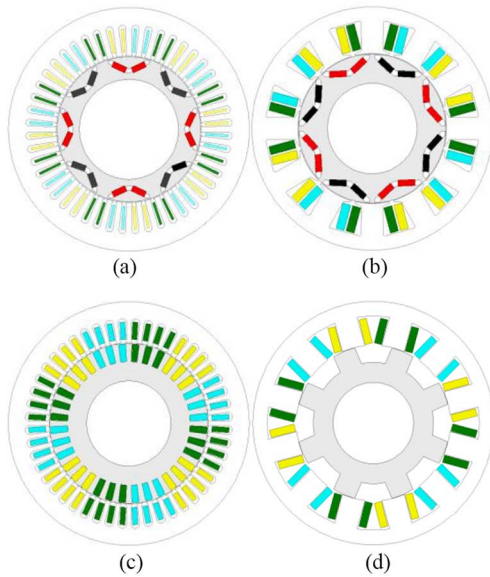
Fig. 1. Cross-section view of: (a) 48/8 IPMSM; (b) 12/8 IPMSM; (c) 48/36 IM; and (d) 12/8 SRM.

equivalent circuit design), Maxwell (static and transient FEA design), and Workbench (mechanical vibration analysis), which can be treated as consistent and is a widely accepted method by industrial [8]. This paper is organized into several sections. Section II identifies motor design inputs and control criteria. In Section III, design results are compared. Section IV evaluates different motor candidates in terms of efficiency and NVH. Conclusion is finally made in Section V.

II. Motor Design and Control Criteria

Four typical traction motor topologies have been selected in this comparison, including an IPMSM with 48-slot 8-pole (referred to as 48/8 IPMSM), IPMSM with 12-slot 8-pole (referred to as 12/8 IPMSM), IM with 48-slot, 36-rotor bar (referred to as 48/36 IM), and a 12/8 SRM with cross-section view shown in Fig. 1. Transient 2-D analysis is used for achieving the performance curves of 48/8 IPMSM and 12/8 IPMSM while the 48/36 IM uses static 2-D FEA analysis. For 12/8 SRM, transient 2-D analysis in Maxwell is used with circuit-field coupling method. Vibration analysis and results are acquired through Workbench 3-D analysis. For a fair comparison, all the motors are designed to share the same outer stator diameter, steel lamination.

Designing specific motor for EV and HEV application, there are many considerations such as torque-speed profile, torque ripple requirements, inverter output power capability, dc-link voltage variations, total weight, and cost [8], [11]. The required peak and continuous torque-speed envelope should be defined according to different driving cycle requirements such as UDDS and US06 with respect to mechanical constraints of the vehicle including vehicle mass, wheel inertia, gearbox ratio, and efficiency. The detailed procedure can be found in [12] and [13]. As shown in Fig. 2, the maximum torque at base speed (point A) determines the vehicle performance at starting or
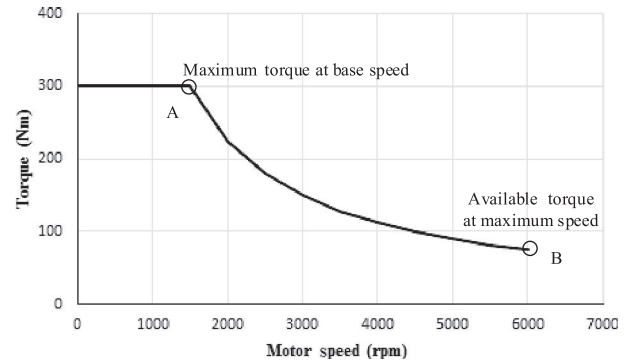

Fig. 2. Target torque-speed envelop for comparison.

climbing hills, whereas the available torque at maximum speed (point B) limits the vehicle speed at the highways. Transient overload capability of the motor is limited by the inverter [8].

In this study, the 48/8 IPMSM used in the second generation of Toyota Prius [14] was selected as the baseline motor. The torque-speed envelope shown in Fig. 2 can be acquired from [15] where peak torque is 300 Nm up to base speed of 1500 rpm and high torque of 60 Nm achieved at maximum speed of 6000 rpm. Moreover, the maximum dc-link voltage for Prius is 500 V. The other three motor candidates are designed under the same specification and requirements; thus, it generates a reasonable and relatively fair comparison between different topologies. Other geometries such as stack length are optimized to meet this requirement.

Special control strategy of different motor topologies should be optimized to achieve a high efficiency. Motor control relates to one fundamental question: what kind of current should be applied to the winding to simultaneously satisfy the performance and efficiency requirement. Since traction motors for electric vehicle application operate in highly nonlinear conditions [16], such as saturation and cross coupling, using lookup table [17] may be the optimal solution. Building the lookup table to find the optimal current trajectories involves several steps as following. The 48/8 IPMSM is used for explaining the method.

Step 1) Injecting currents into the winding, motor parameters need to be extracted, especially the flux linkage. Figs. 3 and 4 show Prius motor's d- and q-axes flux linkage at different current levels, respectively.

Step 2) Based on the flux linkage information, optimal operating plane needs to be generated, as shown in Fig. 5. This plane is bounded by current limit circle, maximum torque per ampere (MTPA) curve, and maximum torque per voltage (MTPV) curve. Constant torque loci (black curves) and voltage ellipse (blue dotted curves) have also been shown.

Step 3) For each given torque-speed requirement, optimal current i_d and i_q can be determined by using extrapolation and interpolation techniques. Fig. 6 shows the unique combination of reference current i_d and i_q for each torque-flux, i.e., torque-speed requirements. The step size for torque command is 15 Nm and for flux command is 0.007 Wb.
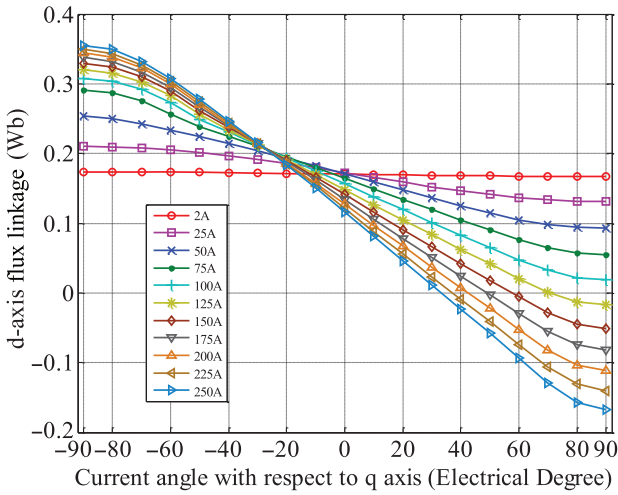
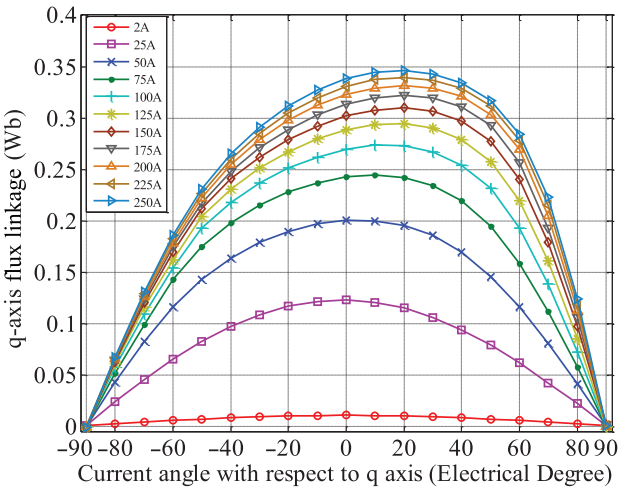Fig. 3. Calculated *d*-axis flux linkage at different current levels.

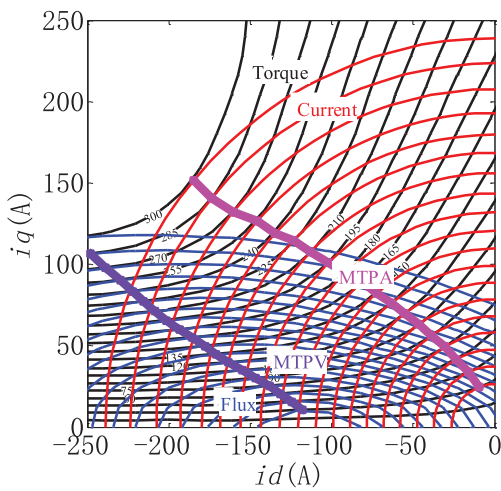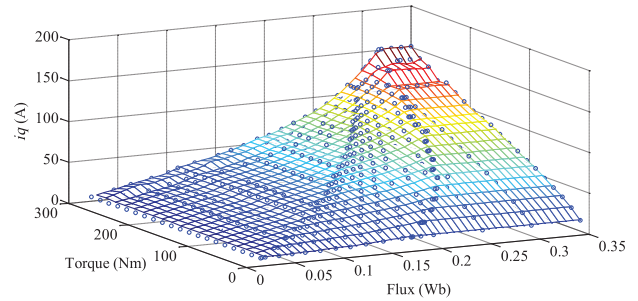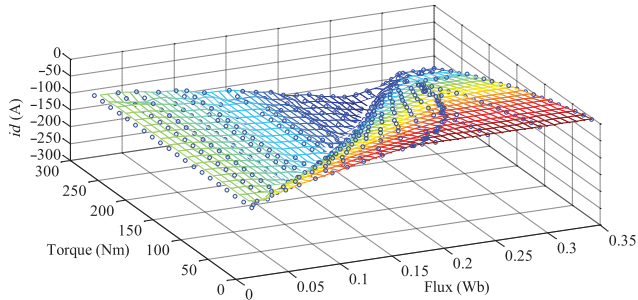Fig. 4. Calculated *q*-axis flux linkage at different current levels.

Fig. 5. Optimal operating plane for the 48/8 IPMSM.

(a)

(b)

Fig. 6. (a) Reference current i_q versus torque and flux command. (b) Reference current i_d versus torque and flux command.

TABLE I
SPECIFICATIONS OF MOTOR TOPOLOGIES

Parameter		48/8 IPMSM	12/8 IPMSM	48/36 IM	12/8 SRM
Maximum dc-link voltage (V)		500			
Peak power (kW)		50			
Maximum rotational speed (rpm)		6000			
Peak torque (Nm)		300			
Designed rated operating point	Torque (Nm)	100*	120	90	100
	Speed (rpm)	3000*	2500	3300	3000
Pole pairs		4	4	2	–
Stator outer diameter (mm)		269			
Stator inner diameter (mm)		161.9	166	177.9	172
Rotor inner diameter (mm)		110	100	94	90
Stack length (mm)		83.82	83.82	108	105
Air gap length (mm)		0.73	0.7	0.45	0.5
Rotor inertial moment (kg m²)		0.042	0.047	0.081	0.069
Armature core weight (kg)		17.3	13.75	17.25	17.83
Armature copper weight (kg)		5.9	8.13	13.05	15.39
Rotor core steel weight (kg)		5.37	6.7	10.06	9.24
Magnet weight (kg)		1.23	1.3	–	–
Rotor bar and ring (kg)		–	–	8.43	–
Total weight (kg)		29.8	30	48.8	42.5
Magnet type		N36Z_20			
Magnet size (mm)		18.9*6.5	19.1*6.8	NA	
Characteristic current (A)		105	98		
Steel lamination		M19-29G			

*Estimated value.

III. DESIGN RESULTS AND COMPARISON

Table I summarizes the specification of four candidate topologies. The outer diameter of stator is kept to be the same as 269 mm. The maximum dc-link voltage for all motors is 500 V. To meet the torque requirement, the stack length of IM and SRM is extended to 105 and 108 mm, respectively. It should be noted that the rated operating point of 48/8 IPMSM is selected by estimating the experimental results from [15] but it may not be accurate because the data were protected by intellectual property.
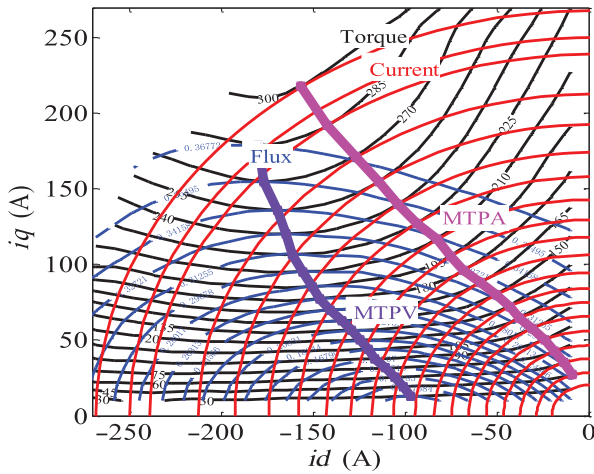
Fig. 7. Optimal operating plane for the 12/8 IPMSM.

Fig. 8. Field orientation in rotor flux reference frame and slot information.

A. 48/8 IPMSM

Prius 48/8 IPMSM has several unique design features.
1) Stator teeth are deep and wide so as to avoid saturation and increase saliency.
2) Permanent magnets are arranged in V shape optimally to take advantage of reluctance torque and reduce no load iron loss.
3) Prius motor's dominant vibration mode order (which is equal to the greatest common divisor (GCD) between the number of slots and the number of poles) is pretty high so that the resonance with stator's low mode orders is successively avoided.

B. 12/8 IPMSM

The designed 12/8 IPMSM has the same stack length as that of Prius motor. Following points are addressed during the design process.
1) Nominal operating point was chosen to be 120 Nm at 2500 rpm. Flux density in the stator teeth and yoke was designed to be lower than the knee point of B–H curve of lamination. This would help avoid saturation at overload torque. Current density is kept around 6 A/mm^2 for nominal operating point.
2) More permanent magnets were utilized to increase electromagnetic torque component and PMs were arranged in V shape optimally to minimize torque ripple.
3) Stator slot geometry was optimized to lower overall loss by balancing copper and iron losses.
4) Number of turns per coil was optimized to meet peak torque-speed envelope requirement.

Fig. 7 shows the optimal operating plane for the 12/8 IPMSM. Its characteristic current is about 100 A, which is close to Prius motor's 105 A. For 12/8 IPMSM, MTPA line shifts away into $i_q > i_d$ region, as shown in Fig. 7, which means that the electrometric torque dominates. The torque equation of IPMSM is given by [18]

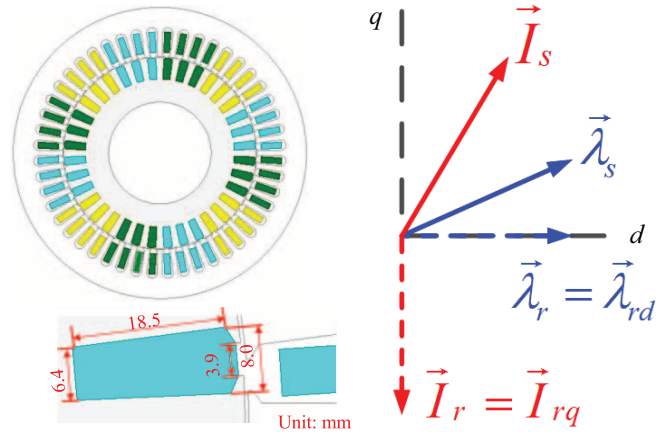$$T_p = \frac{m}{2} \frac{P}{2} \left(\lambda_{d,PM} i_q + (L_d - L_q) i_d i_q \right). \tag{1}$$

The first part is electrometric torque and the second part is reluctance torque. For IPMSM with fractional slot concentrated winding such as 12/8 IPMSM, it exhibits low saliency which means L_q/L_d is low so that it is easier to saturate at high current region. Therefore, reluctance torque cannot be fully utilized and electromagnetic torque dominates. In contrast, IPMSM with integer slot distributed winding, such as the 48/8 IPMSM used in Prius, has a higher saliency and utilizes reluctance torque more effectively as shown in Fig. 5.

C. 48/36 IM

Compared to the 48/8 IPMSM, 48/36 IM has longer stack length (108 mm) to achieve large torque and high-efficiency design. FEA transient analysis of induction machine requires significant computation time, especially when the excitation is provided by a voltage source. The current needs several periods to reach steady state. To reduce computation time, method presented in [19] has been adopted as reference. Instead of applying voltage in stator winding while keeping rotor copper bar short-circuited, both stator and rotor currents are injected into stator winding and rotor copper bar individually. In the rotor flux reference frame, when the field-oriented condition (FOC) is satisfied, which means only the d-axis rotor flux exists while q-axis rotor flux is zero, i.e., $\overrightarrow{\lambda}_r = \overrightarrow{\lambda}_{rd}$ as shown in Fig. 8. In other words,

$$i_{rq} = -\frac{L_M}{L_r} i_{sq}. \tag{2}$$

The fast FEA modeling approach based on current excitation consists of two parts.

1) Magnetostatic FEA Modeling: Both stator and rotor currents are injected into the stator winding and rotor copper bar separately. The q-axis currents are adjusted iteratively until FOC is satisfied as shown in (2). Machine parameters including stator inductance L_s, rotor inductance L_r, and mutual inductance L_m can be calculated based on current and flux information. Slip speed related to stator currents (i_{sq}/i_{sd}) and rotor time constant (L_r/R_r) can also be obtained. Obviously, the calculation takes saturation effect into account.
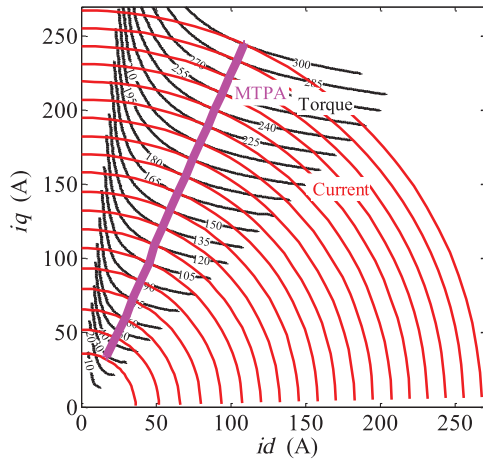
Fig. 9. Optimal operating plane for the 48/36 IM.

Fig. 10. Flux linkage and static torque profile at different rotor position.

2) Transient FEA Modeling: Both the stator and rotor are kept stationary. Stator currents with frequency f_e are injected into the stator winding. Rotor currents with frequency f_e are also injected into rotor copper bar with amplitude indicated in (1). Inductances (L_s, L_r, L_m) varying with currents have been calculated in magnetostatic FEA.

Several iterations are needed to extract IM's parameters as described in magnetostatic FEA. However, this fast FEA modeling method saves significant computation time in predicting IM's performance over the entire torque-speed range.

At the maximum speed of 6000 rpm, the magnetizing reactance $X_m >> R_s$ and stator reactance $X_{ls} >> R_s$, by neglecting the stator resistance R_s, the induction machine's pull-out torque can be approximately expressed as [20]

$$T_p = \frac{3}{2}\frac{P}{2}\frac{V^2}{\omega(R_{\mathrm{TH}} + \sqrt{R_{\mathrm{TH}}^2 + (X_{\mathrm{TH}} + X_{lr})^2})}$$
$$\approx \frac{3}{2}\frac{P}{2}\frac{V^2}{\omega^2(L_{ls} + L_{lr})} \tag{3}$$

where V is the supply voltage, L_{ls} is the stator leakage inductance, L_{lr} is the rotor leakage inductance, and P is the number of poles which equals 4.

According to (3), as the speed approaching the maximum speed, the pull-out torque will be inversely proportional to the square of the speed. Thus, to improve torque performance at high-speed, rotor slot is designed to be wider and shallower and number of turns per coil is decreased reasonably [21]–[23]. This results in reduced rotor leakage inductance and enhanced pull-out torque. Optimized rotor slot shape and dimension are shown in Fig. 8. Rotor slot height, bottom width, top width, and rotor slot open width are 18.5, 6.4, 8, and 3.9 mm, respectively.

Fig. 9 shows the optimal operating plane for the 48/36 IM. Optimal stator current trajectories can be obtained following the procedure for IPMSM.

D. 12/8 SRM

Design optimization is focused on the following parts.
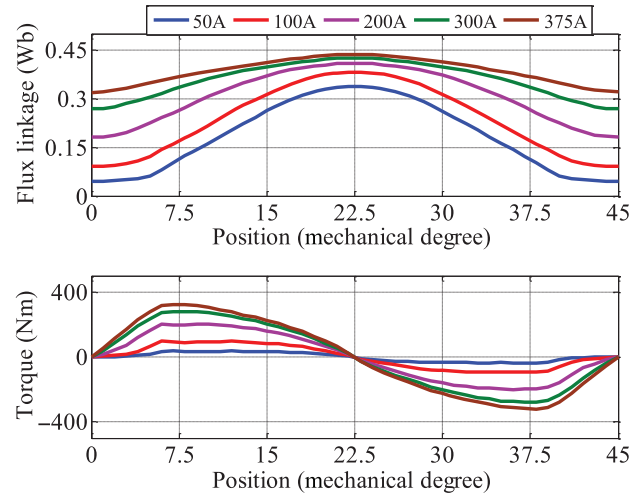1) Nominal operating point was chosen to be 100 Nm at 3000 rpm. Flux density in stator teeth and yoke was designed to be lower than the knee point of B–H curve of lamination. Stack length was increased to 105 mm to meet torque requirement.
2) Number of turns per coil was optimized to meet torque-speed envelope requirement such as peak torque up to base speed (1500 rpm) and high toque at maximum speed (6000 rpm) [24].
3) The turn-ON angle, turn-OFF angle, and current amplitude can be used to optimize SRM efficiency over full torque-speed range [24], [25]. To keep it simple, the control strategy was designed as follows. At low speed, current chopping control was adopted with fixed turn-ON angle and fixed dwell angle; at medium speed, current chopping control is adopted with fixed dwell angle and variable turn-ON angle; at further high speed, angular position control (single pulse operation) with advancing turn-ON angle and fixed turn-OFF angle is adopted. Several iterations and sweeps were performed in the RMxprt and Maxwell environment to find the maximum efficiency for each torque-speed point. Fig. 10 shows the flux linkage and static torque profile at different rotor positions.

IV. COMPARATIVE EVALUATION

A. Efficiency Map

The efficiency maps are presented in Fig. 11. The efficiency calculation is defined as

$$\eta = \frac{P_{\mathrm{out}}}{P_{\mathrm{out}} + P_{\mathrm{loss}}} \tag{4}$$

where P_{loss} include iron loss, copper loss, and permanent magnet (PM) losses but exclude frictional or mechanical loss. Iron core loss can be calculated by means of Steinmetz equation [26]

$$P_{\mathrm{loss}}(W/kg) = K_h(f_e)B^2 f_e + K_c(f_e)B^2 f_e^2 + K_e(f_e)B^{1.5} f_e^{1.5} \tag{5}$$

where K_h, K_c, and K_e represent frequency-dependent coefficients of hysteresis, eddy current, and excess losses. B is the amplitude of flux density and f_e is the electrical frequency.
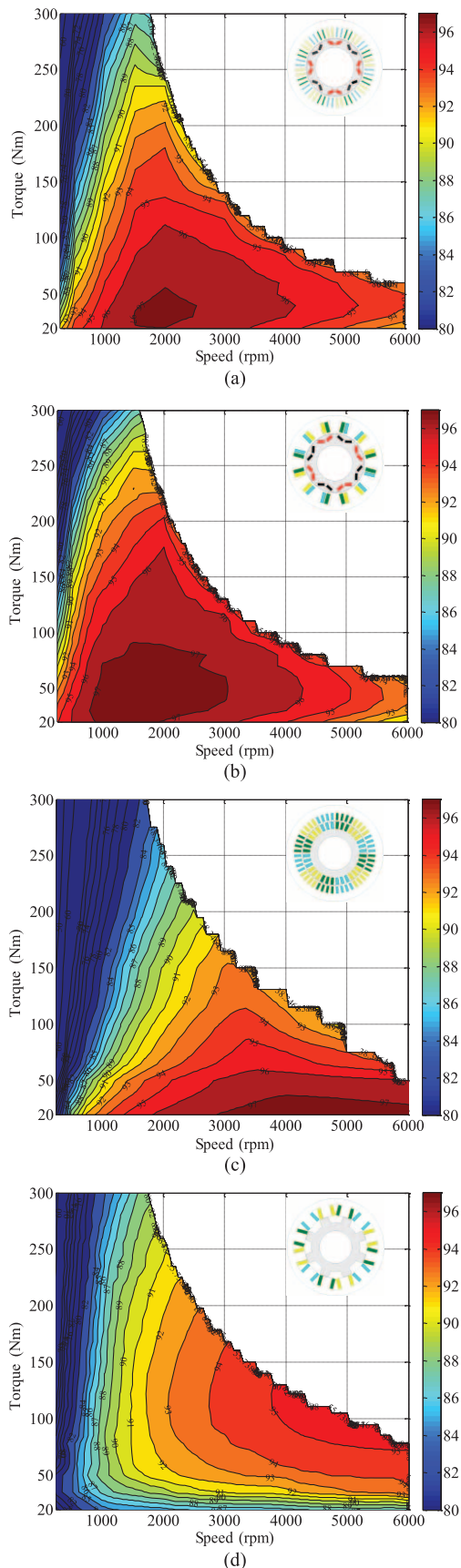
Fig. 11. Efficiency map from top to bottom. (a) 48/8 IPMSM. (b) 12/8 IPMSM. (c) 48/36 IM. (d) 12/8 SRM.

To calculate copper loss, it is assumed that stator windings are set at $100\,^{\circ}$C and rotor bar of IM is set at $140\,^{\circ}$C. The PM temperature is assumed to be lower than $150\,^{\circ}$C where there is little irreversible demagnetization effect of the permanent magnet [8]. The experiment results of 48/8 IPMSM in [15] also prove this assumption. Additional thermal design would be necessary to maintain the PM temperature. To maximize the efficiency, the control strategy is carefully chosen as described in Section II.

For IPMSM and IM, efficiency calculation is done by transient 2-D-FEA analysis for every 10 Nm and 500 rpm. For SRM, circuit-field coupling method [27] is used to perform current chopping control and angular position control.

Efficiency maps show the region where the highest efficiency locates at. For 48/8 IPMSM, the highest efficiency is 97% and locates around 2000 rpm and between 20 and 50 Nm. As stated in [28], the peak torque-speed envelop shows a good consistency with the result provided in [15] with error ranging from approximate 5% to 10% between simulated values and the experimental results at different speed points. For 12/8 IPMSM, the highest efficiency locates in similar region but with expanded area. Due to its concentrated winding structure, 12/8 IPMSM with lower copper loss has 0.5%–1% higher efficiency than that of 48/8 IPMSM in most regions. This is favored to EV and HEV application, as most frequently operation lies between low- and medium-speed range. However, at speeds above 5000 rpm, 12/8 IPMSM loses this advantage due to the penalty from PM eddy current loss. For 12/8 IPMSM topology, the dominant MMF space harmonic orders and corresponding per unit amplitudes are 1st (100%), 2nd (50%), 4th (25%), 5th (20%), and 7th (14.29%).

Higher order harmonics with relatively large amplitude rotate relative to the rotor, thereby contributing to high-eddy current loss at high speed. Regarding 48/8 IPMSM topology, the dominant MMF space harmonic orders and corresponding per unit amplitudes are 1st (100%), 5th (5.39%), 7th (3.83%), and 11th (9.09%).

48/36 IM offers efficiency over 96% at high-speed ($>$3000 rpm) benefiting from: 1) low copper loss by decreasing d-axis current; 2) low core loss due to low pole number. It is important to keep in mind that we use fast FEA method to model induction machine. Any rotor or stator slot harmonic relating to the motion is not considered as the rotor is kept stationary. Therefore, iron loss calculation is underestimated. Below base speed and near peak torque region, efficiency is as low as 60%. Thus, attention should be paid on how to dissipate this loss.

Fig. 11(d) shows the efficiency map of 12/8 SRM. The torque-speed envelop is shaped to represent power less than 60 kW only. However, SRM does have the ability to operate at higher speed by advancing turning-ON angle or continuous conduction operation. The maximum efficiency 95% appears only after 3800 rpm in medium torque ($\sim$100 Nm) region.

Detail comparison of loss and efficiency at typical operating points is given in Appendix I.
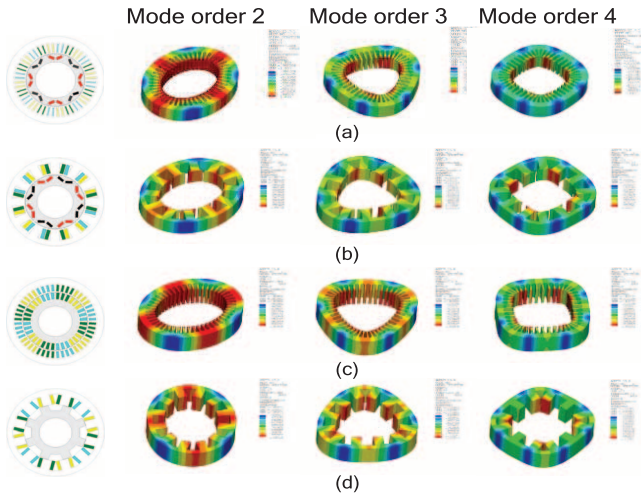
Fig. 12. Modal shapes. (a) 48/8 IPMSM. (b) 12/8 IPMSM. (c) 48/36 IM. (d) 12/8 SRM.

TABLE II
NATURAL FREQUENCIES (Hz) OF STATOR

Mode order	48/8 IPMSM	12/8 IPMSM	48/36 IM	12/8 SRM
0	5078.58	4690.073	5603.149	4759.663
2	612.914	388.322	650.335	422.345
	617.424	*377.051*	*657.966*	*461.445*
3	1628.547	1033.169	1758.513	1131.144
	1619.057	*991.088*	*1770.898*	*1229.461*
4	2889.007	1835.028	3181.872	2023.909
	2770.638	*1730.332*	*3173.837*	*2185.723*
5	4289.773	2727.652	4816.306	3029.644
	3719	*2435.356*	*4607.2*	*3155.007*

Number with italic and underline is from Hoppe's equation number without italic and underline is from ANSYS.

B. NVH

1) Modal Analysis: Fig. 12 shows the mode shapes of the stator calculated in ANSYS workbench environment [28], [29]. Only circumferential modes [29] are plotted in Fig. 12. Table II shows the comparison of natural frequencies obtained from ANSYS and analytical calculation based on Hoppe's equation [28]. The two results agree well for low mode orders.

Natural frequencies (unit: Hz) of 12/8 IPMSM's stator are relatively low due to its thinner yoke thickness and short stack length.

2) Radial Force: Electromagnetic radial force density acting on stator teeth causes deformation of stator yoke. Based on Maxwell stress tensor method, it is calculated as follows [28]–[32]:

$$f_{\text{rad}}(\theta, t) = \frac{B_r^2(\theta, t) - B_t^2(\theta, t)}{2\mu_0} \tag{6}$$

where B_r and B_t are the radial and tangential components of the air gap flux density, μ_0 is the permeability of air, θ is the angular position, and t is the time. Radial force density can also be expressed by Fourier series as shown in the following equation:

$$f_{\text{rad}}(\theta, t) = \sum_{m,n} \hat{F}_{m,n} \cos(m\theta + n\omega_e t + \psi_{mn}) \tag{7}$$
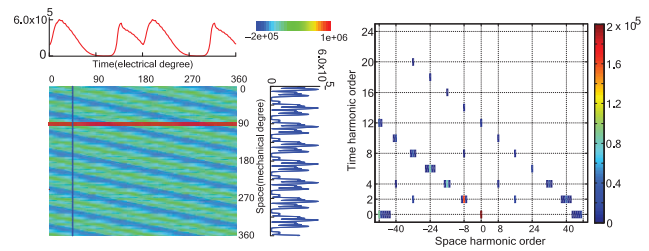

Fig. 13. Radial force density distribution and its spectrum of 48/8 IPMSM at 60 Nm 2500 rpm (MTPA point).

where $\hat{F}_{m,n}$ is the amplitude; m is the space harmonic order which determines force distribution shape; n is the time harmonic order which determine the number of times per second the force repeats itself; $\omega_e = 2\pi f_e$ is the rotor angular velocity in electrical degree.

Fig. 13 shows the evolution of radial force density over time and space both in one period for 48/8 IPMSM. The motor operates at MTPA point (60 Nm, 2500 rpm, $i_d = -30$ A, $i_q = 39$ A). The horizontal line represents variation in time domain at one random location, whereas the vertical line represents variation in space domain at one random time. By applying bidimensional fast Fourier transformation (FFT), its spectrum in terms of space and time harmonic order can be identified which is shown on the right. The amplitude (unit: N/m²) is represented by color block. For better visualization, only amplitudes larger than 2000 N/m² are shown by color block.

Space harmonic order and frequency under load condition are in the form as follows (Appendix II):

$$[m, nf_e] = [-2k_p p \pm k_s N_s/2, 2k_p f_e],$$
$$k_p = 0, 1, 2, \ldots; \quad k_s = 0, 1, 2, \ldots \tag{8}$$

Clearly, the space harmonic order is modulated by the combination of pole and slot numbers. Negative space harmonic order means the deformation rotates in opposite direction [28].

Fig. 14 shows the radial force density spectrum under load conditions: 50 Nm at 1000 rpm and 50 Nm at 5000 rpm. For 48/8 IPMSM, radial force density $[0, 0f_e]$ has the largest amplitude. However, this excitation only causes a time invariant deformation over stator outer periphery, thus vibration velocity induced is negligible. Radial force density $[m, nf_e]$ with $m > 8$ can be neglected.

As from a vibration point of view, higher vibration mode order (which is equal to space harmonic order) contributes little to the stator deformation due to the fact that vibration amplitude is inversely proportional to the fourth power of mode order [28]. For 48/8 IPMSM, dominant radial force components are $[-8, 2f_e]$ $[0, 12f_e]$. For 12/8 IPMSM, dominant radial force components are $[-4, 2f_e]$ $[0, 6f_e]$. For 48/36 IM, dominant radial force component is $[-4, 2f_e]$. Component with space harmonic order 0 cannot be taken into account in Fig. 14(c) as the rotor is kept stationary in the FEA calculation. For 12/8 SRM, dominant radial force component is $[4, f_e]$.

For IPMSM and IM at high speed, radial force amplitude is attenuated as the field is weakened for speed extension.

For the SRM, harmonic components are much more than the other motors, especially relating to space harmonic order 0.

Fig. 15. Stator core deformation under different load conditions. (a) 48/8 IPMSM. (b) 12/8 IPMSM. (c) 48/36 IM. (d) 12/8 SRM.

TABLE III
MAXIMUM DEFORMATION (μm) OF STATOR

Torque	Speed	48/8	12/8	48/36	12/8
(Nm)	(rpm)	IPMSM	IPMSM	IM	SRM
50	1000	0.584	5.17	0.727	5.19
50	5000	0.495	3.80	0.645	4.72

Fig. 15 shows the total deformation of stator core under different load conditions. Under the load 50 Nm at 1000 rpm, 48/8 IPMSM has the minimum stator core deformation with $5.84e^{-7}$ m, whereas 12/8 IPMSM and 12/8 SRM have the maximum deformation with $5.17e^{-6}$ m. Under the load 50 Nm at 5000 rpm, 12/8 SRM has the maximum deformation with $4.72e^{-6}$ m due to single pulse operation. For the other three motors, deformation is smaller than those under 50 Nm at 1000 rpm condition due to field weakening control at high speed. Table III compares the maximum deformation of stator under different load conditions.
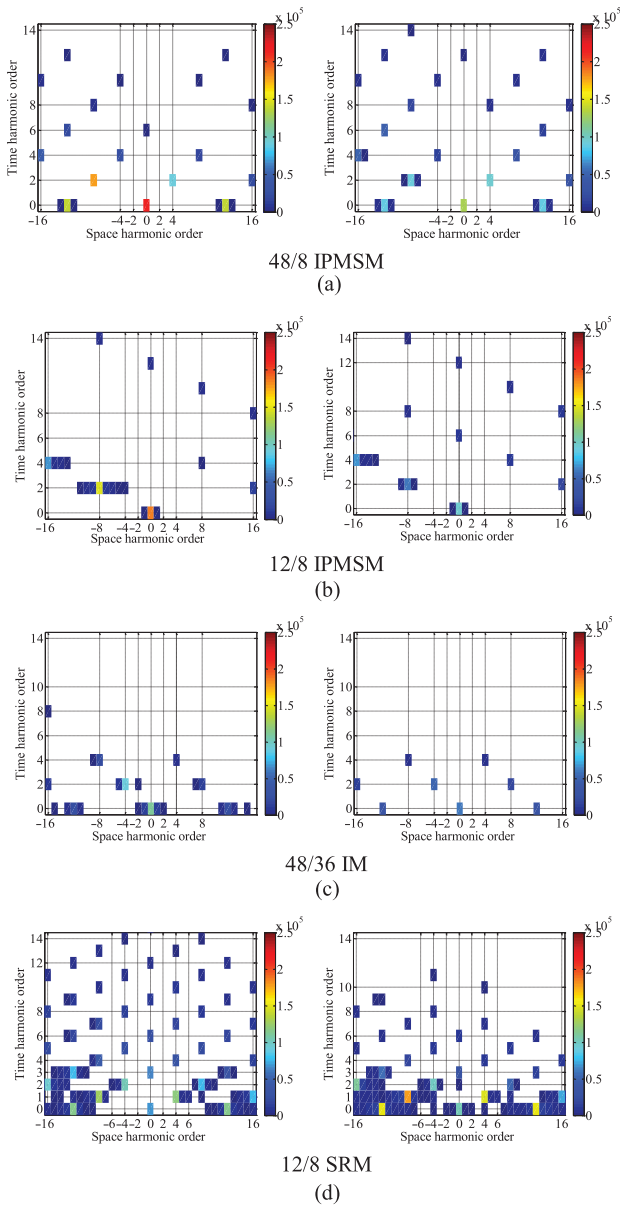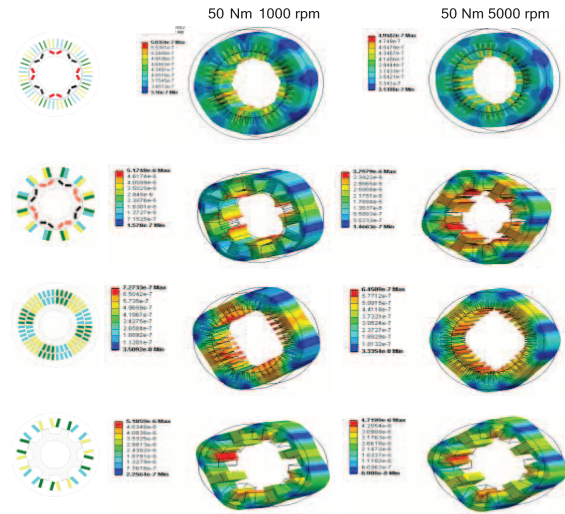

Fig. 14. Radial force density spectrum under different load conditions. Left column: 50 Nm 1000 rpm. Right column: 50 Nm 5000 rpm. (a) 48/8 IPMSM. (b) 12/8 IPMSM. (c) 48/36 IM. (d) 12/8 SRM.

This is due to discontinuous current operation which yields much more nonsinusoidal flux in the air gap.

FEA results in Fig. 14 show that the lowest space harmonic orders except zero for different machines are 8 (48/8 IPMSM), 4 (12/8 IPMSM), 4 (48/36 IM), and 4 (12/8 SRM). This agrees well with analytical analysis shown in Appendix II. The conclusion is also valid for both low and high speeds, which indicates that control strategy for high speed will not change the lowest space harmonic order, but only amplitude. From a vibration point of view, higher space harmonic order (which is equal to vibration mode order) contributes little to the stator deformation due to the fact that vibration amplitude is inversely proportional to the fourth power of mode order [33]–[35]. Therefore, 48/8 IPMSM should have the quietest operation. It is important to keep in mind that additional radial force with low space harmonic order would be introduced once the excitation mode changes, e.g., during six step operation [28].

V. CONCLUSION

This paper performs the side-by-side comparison and assessment of four candidate motor topologies for traction application in for EVs and HEVs. The topologies considered include interior permanent magnet synchronous motor (IPMSM), IM, and SRM. Comparison criteria include performance, efficiency, and vibration. Also, a fast FEA modeling approach has been developed to predict the IM's performance over the full torque-speed range and the control strategy is carefully designed to meet performance and efficiency requirement simultaneously. NVH study including modal analysis and transient analysis is also provided. Comparative evaluation indicates the following.

1) 48/8 IPMSM and 12/8 IPMSM offer efficiency as high as 97%. 12/8 IPMSM has lightly higher efficiency at low speed, but above 5000 rpm, this advantage is lose as PM eddy current losses increase by 50 times, about 1000 W. 48/36 IM delivers the highest efficiency 96% at high speed but it has the widest low efficiency region at low speed due to copper loss. 12/8 SRM has concentrated

TABLE IV
COMPARISON OF LOSS AND EFFICIENCY AT TYPICAL OPERATING POINTS

48/8 IPMSM						
Torque (Nm)	Speed (rpm)	I_d/I_q (A)	Core loss (W)	PM loss (W)	Copper loss (W)	Effi (%)
30	3000	−20.5/20.9	173.0	0.098	96.04	97.14
50	1000	−18.7/36.3	52.7	0.012	186	95.51
50	5000	−80.2/21.1	552.4	1.328	766.6	95.06
300	1500	−184.8/151.6	185.7	5.7	6376.7	87.43

12/8 IPMSM						
Torque (Nm)	Speed (rpm)	I_d/I_q (A)	Core loss (W)	PM loss (W)	Copper loss (W)	Effi (%)
30	3000	−21/16.2	161.3	37.4	61.4	97.23
50	1000	−10.2/30.1	65.5	4.2	87.9	96.99
50	5000	−65.4/23	298.5	651	418.1	94.89
300	1500	−149.2/222.4	221.4	182.3	6238	87.31

48/36 IM						
Torque (Nm)	Speed (rpm)	I_d/I_q (A)	Core loss (W)	Rotor copper loss (W)	Stator copper loss (W)	Effi (%)
30	3000	16.2/34.2	97.6	95.1	121.5	96.83
50	1000	24.2/51.3	35.9	214.9	273.8	91.04
50	5000	11.1/75	110.8	458.1	488.7	96.25
300	1500	108.2/44.6	74.2	5019.1	6083.1	79.02

12/8 SRM						
Torque (Nm)	Speed (rpm)	I_{peak} (A)	Turn ON turn OFF electric angle	Core loss (W)	Copper loss (W)	Effi (%)
30	3000	60	0–120	886.2	163.6	90.99
50	1000	80	0–120	379.1	282.9	88.47
50	5000	80	18–138	1346.2	296	93.8
300	1500	350	25–145	1019.2	6222.7	86.13

winding with low resistance but may need more current to deliver the same torque. 12/8 IPMSM has concentrated winding with low resistance but may need more PM material to meet torque requirement. IM and SRM have lower peak power density, i.e., 50 kW/48 kg and 50 kW/42 kg respectively, comparing with 50 kW/30 kg for IPMSM.

2) Stator geometry, pole/slot combination, and control strategy differentiate NVH performance. Higher mode order will generate smaller vibration. For the same 12/8 topology, the SRM has severe vibration deformation than that of IPMSM, as the former operates in discontinuous current mode. Research is currently underway including optimization of the lamination material for the candidate motor topologies.

APPENDIX I

Table IV shows a comparison of loss and efficiency at typical operating points.

APPENDIX II

Stator slot number, rotor slot number, and pole number play an important role in NVH. Space harmonic order m or mode order of radial force density causing the vibration can be calculated as follows.

1) *IPMSM*

$$m = v \pm u$$
$$v = (3k_1 + 1)P/d \quad (q = b + c/d, d = \text{even}, k_1 = \pm 1, \pm 2, \ldots)$$
$$v = (6k_1 + 1)P/d \quad (q = b + c/d, d = \text{odd}, k_1 = \pm 1, \pm 2, \ldots)$$
$$u = (2k_2 + 1)P/2 \quad (k_2 = 1, 2, \ldots)$$

where q is the slot number per pole per phase, v is the harmonic order due to stator magneto-motive-force (MMF), and u is the harmonic order due to rotor MMF. The lowest mode order except 0 for 48/8 IPMSM is 8. The lowest mode order except 0 for 12/8 IPMSM is 4.

2) *IM*

$$m = v \pm u$$
$$v = (6k_1 + 1)P/2 \quad (k_1 = \pm 1, \pm 2 \ldots)$$
$$u = k_2 z_2 + P/2 \quad (k_2 = \pm 1, \pm 2 \ldots)$$

where z_2 is the rotor slot number. Keeping pole number P to be 4, the lowest mode number except 0 for 48/42, 48/38, 48/36 topologies are 2, 2, and 4, respectively. Comparing with the other two topologies, 48/36 design exhibits relatively lower noise and vibration due to higher mode order.

3) *SRM*

$$m = z_1/r$$

where z_1 is the number of stator poles and r is the number of phases. The lowest mode order except 0 for 12/8 SRM is 4.

REFERENCES

[1] M. Zeraoulia, M. Benbouzid, and D. Diallo, "Electric motor drive selection issues for HEV propulsion systems: A comparative study," *IEEE Trans. Veh. Technol.*, vol. 55, no. 6, pp. 1756–1764, Nov. 2006.

[2] I. Boldea, L. N. Tutelea, L. Parsa, and D. Dorrell, "Automotive electric propulsion systems with reduced or no permanent magnets: an overview," *IEEE Trans. Ind. Electron.*, vol. 61, no. 10, pp. 5696–5711, Oct. 2014.

[3] A. Chiba *et al.*, "Torque density and efficiency improvements of a switched reluctance motor without rare-earth material for hybrid vehicles," *IEEE Trans. Ind. Appl.*, vol. 47, no. 3, pp. 1240–1246, May/Jun. 2011.

[4] Z. Q. Zhu and C. C. Chan, "Electrical machine topologies and technologies for electric, hybrid, and fuel cell vehicles," in *Proc. IEEE Veh. Power Propul. Conf.*, 2008, pp. 1–6.

[5] S. S. Williamson, S. M. Lukic, and A. Emadi, "Comprehensive drive train efficiency analysis of hybrid electric and fuel cell vehicles based on motor controller efficiency modeling," *IEEE Trans. Power Electron.*, vol. 21, no. 3, pp. 730–740, May 2006.

[6] T. Finken, M. Felden, and K. Hameyer, "Comparison and design of different electrical machine types regarding their applicability in hybrid electrical vehicles," in *Proc. 18th Int. Conf. Elect. Mach.*, 2008, pp. 1–5.

[7] D. G. Dorrell, A. M. Knight, L. Evans, and M. Popescu, "Analysis and design techniques applied to hybrid vehicle drive machines -Assessment of alternative IPM and induction motor topologies," *IEEE Trans. Ind. Electron.*, vol. 59, no. 10, pp. 3690–3699, Oct. 2012.

[8] G. Pellegrino, A. Vagati, B. Boazzo, and P. Guglielmi, "Comparison of induction and PM synchronous motor drives for EV application including design examples," *IEEE Trans. Ind. Appl.*, vol. 48, no. 6, pp. 2322–2332, Nov./Dec. 2012.

[9] J. Goss and M. Popescu, "A comparison of an interior permanent magnet and copper rotor induction motor in a hybrid electric vehicle application," in *Proc. IEEE Elect. Mach. Drives Conf. (IEMDC)*, May 2013, pp. 220–225.

[10] H. Neudorfer and N. Wicker, "Comparison of three different electric powertrains for the use in hybrid electric vehicles," in *Proc. IET Conf. Power Electron. Mach. Drives*, 2008, pp. 510–514.

[11] J. Wang, X. Yuan, and K. Atallah, "Design optimization of a surface-mounted permanent-magnet motor with concentrated windings for electric vehicle applications," *IEEE Trans. Veh. Technol.*, vol. 62, no. 3, pp. 1053–1064, Mar. 2013.

[12] P. Morrison, A. Binder, B. Funieru, and C. Sabirin, "Drive train design for medium-sized zero emission electric vehicles," in *Proc. 13th Eur. Conf. Power Electron. Appl. (EPE'09)*, Sep. 8–10, 2009, pp. 1–10.

[13] G. Choi and T. M. Jahns, "Design of electric machines for electric vehicles based on driving schedules," in *Proc. IEEE Int. Elect. Mach. Drives Conf. (IEMDC'13)*, May 12–15, 2013, pp. 54–61.

[14] M. Olszewski, "Report on Toyota Prius motor torque capability, torque property, no-load back EMF, and mechanical losses," Oak Ridge Nat. Lab., U.S. Dept. Energy, Oak Ridge, TN, USA, Tech. Rep. ORNL/TM-2004/185, 2007.

[15] M. Olszewski, "Evaluation of the 2004 Toyota Prius hybrid synergy drive system," Oak Ridge Nat. Lab., U.S. Dept. Energy, Oak Ridge, TN, USA, Tech. Rep. ORNL/TM-2006/423, 2005.

[16] K. M. Rahman and S. Hiti, "Identification of machine parameters of a synchronous motor," *IEEE Trans. Ind. Appl.*, vol. 41, no. 2, pp. 557–565, Mar. 2005.

[17] B. Cheng and T. R. Tesch, "Torque feedforward control technique for permanent-magnet synchronous motors," *IEEE Trans. Ind. Electron.*, vol. 57, no. 3, pp. 969–974, Mar. 2010.

[18] S. T. Lee and L. M. Tolbert, "Analytical method of torque calculation for interior permanent magnet synchronous machines," in *Proc. Energy Convers. Congr. Expo. (ECCE'09)*, Sep. 20–24, 2009, pp. 173–177.

[19] L. Alberti, N. Bianchi, and S. Bolognani, "Variable-speed induction machine performance computed using finite-element," *IEEE Trans. Ind. Appl.*, vol. 47, no. 2, pp. 789–797, Mar./Apr. 2011.

[20] S. Jurkovic, J. C. Morgante, K. M. Rahman, and P. J. Savagian, "Electric machine design and selection for General Motors e-Assist Light Electrification Technology," in *Proc. Energy Convers. Congr. Expo. (ECCE'12)*, Sep. 15–20, 2012, pp. 906–913.

[21] A. Harson, P. H. Mellor, and D. Howe, "Design considerations for induction machines for electric vehicle drives," in *Proc. 7th Int. Conf. Elect. Mach. Drives*, 1995, pp. 16–20.

[22] Z. M. Zhao and C. C. Chan, "A novel induction machine design suitable for inverter-driven variable speed systems," *IEEE Trans. Energy Convers.*, vol. 15, no. 4, pp. 413–420, Dec. 2000.

[23] T. Wang, P. Zheng, Q. Zhang, and S. Cheng, "Design characteristics of the induction motor used for hybrid electric vehicle," *IEEE Trans. Magn.*, vol. 41, no. 1, pp. 505–508, Jan. 2005.

[24] K. M. Rahman, B. Fahimi, G. Suresh, A. V. Rajarathnam, and M. Ehsami, "Advantages of switched reluctance motor applications to EV and HEV: Design and control issues," *IEEE Trans. Ind. Appl.*, vol. 36, no. 1, pp. 111–121, Jan./Feb. 2000.

[25] A. Chiba, M. Takeno, N. Hoshi, M. Takemoto, S. Ogasawara, and M. A. Rahman, "Consideration of number of series turns in switched reluctance traction motor competitive to HEV IPMSM," *IEEE Trans. Ind. Appl.*, vol. 48, no. 6, pp. 2333–2340, Nov./Dec. 2012.

[26] J. M. Mille, *Propulsion Systems for Hybrid Vehicles*. Stevenage, U.K.: IET, 2010.

[27] P. Kuo-Peng, N. Sadowski, N. J. Batistela, and J. P. A. Bastos, "Coupled field and circuit analysis considering the electromagnetic device motion," *IEEE Trans. Magn.*, vol. 36, no. 4, pp. 1458–1461, Jul. 2000.

[28] Z. Yang, M. Krishnamurthy, and I. P. Brown, "Electromagnetic and vibrational characteristic of IPM over full torque-speed range," in *Proc. IEEE Elect. Mach. Drives Conf. (IEMDC)*, May 2013, pp. 295–302.

[29] J. F. Gieras, C. Wang, and J. C. Lai, *Noise of Polyphase Electric Motors*. Boca Raton, FL, USA: CRC, 2006.

[30] Y. S. Chen, Z. Q. Zhu, and D. Howe, "Vibration of permanent magnet brushless machines having a fractional number of slots per pole," *IEEE Trans. Magn.*, vol. 42, no. 10, pp. 3395–3397, Oct. 2006.

[31] M. Boesing and R. W. De Doncker, "Exploring a vibration synthesis process for the acoustic characterization of electric drives," *IEEE Trans. Ind. Appl.*, vol. 48, no. 1, pp. 70–78, Jan. 2012.

[32] T. Kobayashi, F. Tajima, M. Ito, and S. Shibukawa, "Effects of slot combination on acoustic noise from induction motors," *IEEE Trans. Magn.*, vol. 33, no. 2, pp. 2101–2104, Mar. 1997.

[33] C. Lin and B. Fahimi, "Prediction of acoustic noise in switched reluctance motor drives," *IEEE Trans. Energy Convers.*, vol. 29, no. 1, pp. 250–258, Mar. 2014.

[34] M. Arata, N. Takahashi1, M. Fujita, M. Mochizuki, T. Araki, and T. Hanai, "Noise lowering for a large variable speed range use permanent magnet motor by frequency shift and structural response evaluation of electromagnetic forces," *J. Power Electron.*, vol. 12, no. 1, pp. 67–74, Jan. 2012.

[35] K. Rahman, M. Anwar, and S. Schulz, "The Voltec 4ET50 electric drive system," *SAE Int. J. Engines*, vol. 4, no 1, pp. 323–337, Apr. 2011.

Zhi Yang received the B.S. degree from Huazhong University of Science and Technology, Wuhan, China, the M.S. degree from Washington State University, Pullman, WA, USA, and the Ph.D. degree from Illinois Institute of Technology, Chicago, IL, USA, in 2005, 2010, and 2014, respectively, all in electrical engineering.

He is currently a Lead Engineer with GE Healthcare, Florence, SC, USA. His research interests include motor control and electromagnetic device development.

Fei Shang (S'14) was born in Tianjin, China, in 1981. He received the B.S. degree in electrical engineering from Beihang University (BUAA), Beijing, China, in 2003, and the M.Sc. degree in power electronics and drives from the University of Birmingham, Birmingham, U.K., in 2004. He is currently pursuing the Ph.D. degree in electrical engineering at the Illinois Institute of Technology, Chicago, IL, USA.

From 2005 to 2010, he was the Product Development Manager with Beijing Accuenergy Technology Co., Ltd., Beijing, China. From 2010 to 2013, he joined Infineon Technologies, Beijing, China, as the Senior Engineer in failure analysis of IGBT module. Since 2013, he has been a Research Assistant with Electric Drives and Energy Conversion Laboratory, Illinois Institute of Technology. His research interests include application of wide band gap devices, high-gain dc–dc converter design, and electric motor control and design.

Ian P. Brown (S'00–M'09) received the B.S. degree in engineering from Swarthmore College, Swarthmore, PA, USA, in 1999, and the M.S. and Ph.D. degrees in electrical engineering from the University of Wisconsin-Madison, Madison, WI, USA, in 2003 and 2009, respectively.

Since 2012, he has been with the Illinois Institute of Technology, Chicago, IL, USA. Previously, he was with the Corporate Technology Center, A.O. Smith Corporation, Milwaukee, WI, USA. His research interests include high-performance electrical drives and the design of electric machines.

Mahesh Krishnamurthy (S'02–M'08–SM'13) received the M.S. degree in electrical engineering from the Missouri University of Science and Technology, Rolla, MO, USA, in 2004, and the Ph.D. degree in electrical engineering from the University of Texas at Arlington, Arlington, TX, USA, in 2008.

Currently, he is an Associate Professor of Electrical Engineering and the Director of the Electric Drives and Energy Conversion Laboratory and Grainger Power Electronics and Motor Drives Laboratory, Illinois Institute of Technology (IIT), Chicago, IL, USA. Before joining IIT, he worked as a Design Engineer with EF Technologies, Arlington, TX, USA. He has coauthored over 60 scientific articles, book chapters and technical reports and has one US patent and three pending. His research interests include design, analysis, and control of power electronics, electric machines and adjustable speed drives for automotive and renewable energy applications.

Dr. Krishnamurthy is a Distinguished Lecturer with the IEEE-Vehicular Technology Society. He was the General Chair for the 2014 IEEE-Transportation Electrification Conference and Exposition. In the past, he has served as the Technical Program Chair for the 2011 Vehicle Power and Propulsion Conference and 2013 IEEE-Transportation Electrification Conference. He has served as the Guest Editor or Associate Editor for several IEEE journals including the Special Section of the IEEE TRANSACTIONS ON VEHICULAR TECHNOLOGY ON SUSTAINABLE TRANSPORTATION SYSTEMS, Special Issue of the IEEE TRANSACTIONS ON POWER ELECTRONICS ON TRANSPORTATION ELECTRIFICATION AND VEHICLE SYSTEMS, and Special Issue of the IEEE JOURNAL OF EMERGING AND SELECTED TOPICS IN POWER ELECTRONICS ON TRANSPORTATION ELECTRIFICATION. He is currently serving as the Deputy Editor-in-Chief for the IEEE TRANSACTIONS ON TRANSPORTATION ELECTRIFICATION and as the on the steering committee of IEEE's Transportation Electrification Community. He was also the Advisor for the Formula Electric Racecar Team at IIT, which won the prestigious Fiat Chrysler Innovation Award at the SAE Formula Hybrid Competition. He was the recipient of the 2006–2007 IEEE VTS-Transportation Electronics Fellowship Award for his contributions.